

Path-integral Monte Carlo simulation of the second layer of ^4He adsorbed on graphite

Marlon Pierce and Efstratios Manousakis

Department of Physics and Center for Materials Research and Technology, Florida State University, Tallahassee, Florida 32306-4350

(Received 13 July 1998; revised manuscript received 5 October 1998)

We have developed a path-integral Monte Carlo method for simulating helium films and apply it to the second layer of helium adsorbed on graphite. We use helium-helium and helium-graphite interactions that are found from potentials which realistically describe the interatomic interactions. The Monte Carlo sampling is over both particle positions and permutations of particle labels. From the particle configurations and static structure factor calculations, we find that this layer possesses, in order of increasing density, a superfluid liquid phase, a $\sqrt{7} \times \sqrt{7}$ commensurate solid phase that is registered with respect to the first layer, and an incommensurate solid phase. By applying the Maxwell construction to the dependence of the low-temperature total energy on the coverage, we are able to identify coexistence regions between the phases. From these, we deduce an effectively zero-temperature phase diagram. Our phase boundaries are in agreement with heat capacity and torsional oscillator measurements, and demonstrate that the experimentally observed disruption of the superfluid phase is caused by the growth of the commensurate phase. We further observe that the superfluid phase has a transition temperature consistent with the two-dimensional value. Promotion to the third layer occurs for densities above $0.212 \text{ atom}/\text{\AA}^2$, in good agreement with experiment. Finally, we calculate the specific heat for each phase and obtain peaks at temperatures in general agreement with experiment. [S0163-1829(99)00705-5]

I. INTRODUCTION

Helium adsorbed on graphite provides an excellent realization of a number of nearly two-dimensional (2D) phenomena. The helium film grows in a succession of distinct, atomically thin layers as the density of the adsorbate increases, and as many as seven such layers may be observed on a well-prepared substrate.¹ Consequently, it is possible to investigate the evolution of each layer's phase diagram. A number of experimental methods have been used for this purpose, including specific heat measurements,^{2-5,1} neutron scattering,⁶⁻⁹ torsional oscillator measurements,^{10,11} and third sound.¹ The phase diagrams of the layers nearest the substrate are rich. Evidence has been found for self-bound fluid phases that are superfluid at low temperatures, a variety of registered solid structures, and incommensurate solid phases. These phases and the coexistence regions that separate them are governed by a delicate balance of quantum effects, such as large zero-point motion and particle permutations, with adatom and substrate interactions.

Much of the early experimental work on the helium-graphite system concentrated on the first adsorbed layer. Several reviews of this work are available.^{2,3,12} On the other hand, until recently, relatively little information was available on the phases of the second and higher layers. This situation has changed dramatically over the last several years. Extensive heat capacity measurements^{4,5} of the first six layers have been performed, and superfluidity in the higher layers has been detected by both torsional oscillator^{10,11} and third sound measurements.¹ Taken together, these experiments indicate that the second layer has a unique phase diagram, with superfluid, commensurate solid, and incommensurate solid phases. No other layer exhibits all three phases.

Motivated by these experiments, we have undertaken a path-integral Monte Carlo (PIMC) simulation of the second adsorbed layer. We identify a liquid (L) phase with an equi-

librium density of $0.1750 \text{ atom}/\text{\AA}^2$, a $\sqrt{7} \times \sqrt{7}$ commensurate triangular solid (C) at $0.1996 \text{ atom}/\text{\AA}^2$, and an incommensurate triangular solid (IC) phase for densities above $0.2083 \text{ atom}/\text{\AA}^2$. All coverage values are for the total adsorbed film. Using the Maxwell construction, we determine coexistence regions between these phases, namely, the gas-liquid (GL), liquid-commensurate solid (LC), and commensurate-incommensurate solid (CIC) phases, at effectively zero temperature. Our calculated phase diagram confirms the idea that the superfluid phase is interrupted by the formation of the commensurate solid.^{10,11,5} We further show that the liquid phase behaves similar to a typical two-dimensional superfluid. We also calculate the specific heat for each phase and find peaks in general agreement with the experimental values. Finally, we observe promotion to the third layer at a coverage in good agreement with experiment. A preliminary report of some of our findings has been published elsewhere.¹³ The present paper expands and extends this work.

This paper is arranged in the following manner. Section I A provides an overview of what is known about the second layer from experiments. In Sec. I B, we review previous simulations of helium films and the related simulation of two-dimensional helium. We point out that none of these simulations, while interesting in their own right, exhibit all the phenomena observed in the second-layer phase diagram. Section II presents the details of our simulation method, which includes particle permutations and realistic particle-particle and particle-substrate interactions. The results of our calculations are presented in Sec. III. We demonstrate the existence of each phase, explain the construction of the second-layer phase diagram, and present calculations of properties for each phase.

A. Experimental overview

Specific heat measurements have formed the basis for constructing the first helium layer's phase diagram, but until

recently, relatively little work was done on the second layer, with a couple of exceptions. Bretz¹⁴ examined this layer under compression of the third and obtained evidence for the melting of the incommensurate second layer solid. The low density range of this layer was explored by Polanco and Bretz.¹⁵ They determined that the compression of the first layer by the growth of the second must be taken into account in order to determine the phases at low second-layer densities. They interpreted their results to indicate that the second layer has gas-liquid coexistence at low coverages.

The heat capacity measurements of Greywall and Busch provide the most extensive investigation of the second-layer phase diagram. They find evidence for four phases: gas, liquid, commensurate solid, and incommensurate solid. These phases are identified in the following manner. At low densities, a low, rounded peak occurs in the heat capacity. This has previously been associated with the liquid phase.¹⁵ At low temperatures, the heat capacity depends linearly on density roughly between 0.13 and 0.16 atom/Å², which is a requirement for coexisting phases,¹⁶ Thus this region can be identified as a gas-liquid coexistence region, with the gas phase having negligible density at the lowest temperatures. Evidence for liquid-commensurate solid coexistence can be found between 0.187 and 0.197 atom/Å². In this region, in addition to the low peak associated with the liquid phase, another, larger peak at a higher temperature can be observed. The location of the larger peak is independent of coverage, suggesting that it may be associated with the melting of a commensurate solid phase. Greywall suggested⁵ that this phase corresponds to the $\sqrt{7} \times \sqrt{7}$ commensurate structure proposed earlier for ³He on graphite.^{17,18} A third coexistence region occurs between 0.2030 and 0.2080 atom/Å², where the commensurate melting peak is accompanied by another, lower temperature peak. This second peak is associated with the melting of an incommensurate solid phase. For coverages from 0.2080 to the beginning of third layer promotion at 0.212 atom/Å², the incommensurate melting peak is the sole feature in the specific heat measurements. Unlike the peak associated with the commensurate phase, the incommensurate melting peak is temperature dependent, occurring at about 1 K at the lowest incommensurate densities, but increasing to about 1.5 K at the density where third layer promotion begins.

The principal limitation on using the heat capacity measurements to determine the phase diagram is that they can only identify phases indirectly, so additional confirmation is desirable. Direct evidence for the incommensurate solid phase comes from neutron scattering,⁷⁻⁹ but no similar evidence exists for the commensurate phase. Apparently, the incommensurate phase can be resolved in these experiments only after some additional compression by the third layer. Consequently, there is no scattering evidence for the commensurate solid, which is replaced by the incommensurate solid before promotion to the third layer begins.

Further insight into the second-layer phase diagram comes from the torsional oscillator measurements of Crowell and Reppy.^{10,11} They detected superfluidity at intermediate densities, which incidentally provided direct evidence that the second layer has a liquid phase. Questions remain about the liquid phase, however, since the apparent onset density is somewhat higher than would be expected from either the

heat capacity measurements or the liquid equilibrium density of purely two-dimensional helium.¹⁹ The range of superfluid coverage also provides additional, although indirect, evidence that a solid phase begins to form above 0.187 atom/Å². Above this density, the superfluid signal vanishes and does not reappear until the third layer. This disappearance coincides almost exactly with the growth of the supposed commensurate solid phase. Apparently, the growing solid phase disrupts the connectivity required to detect superfluidity.

B. Previous simulations

The results of Monte Carlo calculations are often used to help interpret the experimental results discussed above. The simplest way to treat a helium layer is as a purely two-dimensional system, for which there are both zero temperature and finite temperature calculations. Whitlock *et al.*¹⁹ used Green's function Monte Carlo to calculate the equilibrium liquid coverage at zero temperature, obtaining 0.04356 atom/Å². They also determined that 2D helium would solidify, and that the liquid and solid phases coexisted between 0.0678 and 0.0721 atom/Å². More recently, Gordillo and Ceperley²⁰ have investigated the 2D phase diagram at finite temperatures with path integral Monte Carlo. Their low-temperature results are consistent with the zero-temperature calculations. They also determined spinodal lines and found a finite density gas phase at temperatures above 0.75 K. The direct comparison of these results with the second helium layer is limited, since the 2D calculations do not include any substrate features and do not allow the film to spread perpendicularly. As a result, no commensurate solid phase or layer promotion can occur.

Simulations of helium films using realistic models for the graphite substrate have also been performed. Abraham and Broughton²¹ used a path-integral Monte Carlo simulation to investigate the first layer of ³He on graphite. They were able to identify fluid, commensurate solid, domain wall liquid and solid, and incommensurate solid phases. Notably, they determined that particle permutations were unimportant for the first layer for the coverages they investigated, so there was no possibility for superfluidity in the simulation. Experimentally, the phase diagrams for ³He and ⁴He at the densities they simulated are nearly identical, so it is reasonable to conclude that their simulation results also apply to ⁴He. This work was extended¹⁸ to a simulation of the second adsorbed layer of ³He at the $\sqrt{7} \times \sqrt{7}$ commensurate density. Particle permutations were again neglected. It was established that the second-layer commensurate phase was stable for temperatures below 1 K. Very recently, Whitlock *et al.*²² investigated the ground state properties of the first helium layer using a laterally averaged potential for the helium-graphite interaction. They determined the equilibrium liquid coverage and the onset coverage for solidification in the first layer, and determined the coexistence region between these two phases. They also estimated completion densities for the first and second layers, obtaining agreement with the experimental results. They did not take the corrugations of the graphite substrate into account and so did not observe the $\sqrt{3} \times \sqrt{3}$ commensurate solid phase that occurs in the first layer.

Complementary to the calculations discussed above is the work by Clements *et al.*^{23–25} using the hypernetted-chain Euler-Lagrange theory. For 2D helium, this method reproduces the Monte Carlo results¹⁹ for the liquid phase and provides a direct calculation of the chemical potential, third sound, and spinodal points. When applied to layered systems, the theory gives liquid coverage ranges and layering transitions but is not capable of investigating solid phases. For this reason, these calculations are restricted to the third and higher helium layers, and assume that the first two layers form an inert, featureless solid. Also complementary are the path-integral Monte Carlo calculations of Wagner and Ceperley^{26,27} for ⁴He and hydrogen films on crystalline hydrogen. In their helium film simulation, superfluidity and layer-by-layer growth occurred, but the film did not solidify.

As we discussed in Sec. I A, the second layer of ⁴He on graphite is unusual in that it is known experimentally to have both a superfluid liquid and two solid phases, one commensurate and the other incommensurate with the first layer. The simulations discussed above are interesting in their own right, but none have exhibited the three phases seen in the second layer. In order for a simulation to produce these phases, it must possess three features. First, the presence of superfluidity means that particle permutations must be included in the simulation. This is because superfluidity results from permutation cycles of infinite length.²⁸ It is also expected that the boundaries of the phases will be effected by permutations. Second, the commensurate second-layer solid is found to be registered with respect to the first layer, so the effect of first-layer atoms must be taken into account. Third, the attraction of the substrate and first layer on the second must be implemented correctly so that the commensurate phase is replaced by the incommensurate phase before promotion to the third layer begins. In the following section we outline our simulation method, which contains the necessary features to exhibit these three phases.

II. SIMULATION METHODS AND DETAILS

The path-integral Monte Carlo simulation is a powerful tool for studying quantum systems at finite temperatures. By incorporating sampling of particle configurations and particle permutations, both normal and superfluid helium can be simulated.²⁹ If a substrate is added to the simulation, a quantum film will result. The purpose of this section is to describe the modifications that are necessary to add the effects of the substrate into the simulation. The result will be a simulation method that is capable of exhibiting superfluid, commensurate solid, and incommensurate solid phases, as well as layer promotion.

Central to our PIMC method is the approximation used for the high temperature density matrix. It is essential that the starting temperature be made as low as possible so that permutations will be accepted. As we will discuss in this section, the graphite substrate complicates a straight-forward extension of the starting approximation used in bulk simulations. For this reason we will not include sampling of the first-layer atom configurations in the calculation and will concentrate instead on the second layer.

It is essential to include the effect of the first layer on the second, however. We approximate this effect by placing

first-layer atoms on the sites of a triangular lattice at a fixed height above the substrate. This allows us to treat the helium-graphite correlations in a much simpler manner, since the atoms on the second layer are not effected by the corrugations of the graphite substrate. By not sampling first-layer configurations, we are also able to increase the number of second-layer atoms in the simulation. In turn, this allows us to scan second-layer coverages in a sufficiently fine grid to observe coexistence regions. Having a fine grid is particularly important for high second-layer densities, since the liquid-commensurate solid and commensurate-incommensurate solid coexistence regions exist over relatively narrow ranges.

The trade off for using this approach is that we ignore zero-point motion in the first layer. This will cause the second layer to form closer to the first layer and have a narrower density profile.³⁰ Ignoring the response of the first layer to the second is also known to lead to a lowering of the energy of a layer of helium adsorbed onto solid hydrogen.²⁶ However, experimental results indicate that neglecting zero-point motion in the first layer of helium on graphite atoms is a reasonable approximation. First, the Debye temperature of the solid first layer is greater than 50 K, and it may be treated as a 2D Debye solid up to 3 K.³¹ In our simulation, the temperature is as low as 200 mK, and never exceeds 2.2 K, so the first layer is relatively stiff. Second, although the first layer is known to be compressed by the growing second layer, this is most important at low second-layer densities, just after second-layer promotion begins.¹⁵ The coverages studied by Polanco and Bretz¹⁵ are below the range of our simulation. As we shall see, our approach is sufficient to reproduce many of the observed features of the second layer.

A. Path-integral representation of the partition function

We wish to study the problem of a quantum N -particle system in the presence of a substrate. The Hamiltonian for this system may be written as

$$H = -\hbar^2/2m \sum_{i=1}^N \nabla_i^2 + \sum_{i<j}^N v_{2B}(|\mathbf{r}_i - \mathbf{r}_j|) + \sum_{i=1}^N v_{\text{sub}}(\mathbf{r}_i), \quad (1)$$

where v_{2B} is the spherically symmetric two-body potential between particles, and v_{sub} is the external field produced by the substrate. The two-body potential for helium is accurately represented by the Aziz potential.³² Previous path-integral simulations using this potential have proven quite capable of reproducing numerous properties of liquid helium.^{29,33–35} The potential between helium and graphite has been investigated by Carlos and Cole.³⁶ Using helium-scattering data, they evaluated several forms for the helium-graphite potential. In order to write this potential in a pair form, anisotropic terms that effectively enhance corrugation must be included. Of the potentials examined, an anisotropic 6-12 Lennard-Jones potential was found to be preferable, although the form was not uniquely determined. For helium atoms more than 4 Å above the substrate, corrugations are negligible, and the anisotropic potential can be replaced by a laterally averaged potential that depends only on the height of the atom above the substrate.

The statistical mechanics of quantum systems is governed by the density matrix and the partition function. For a system of N bosons at an inverse temperature β , the density matrix is given by

$$\rho(\mathbf{R}, \mathbf{R}'; \beta) = \frac{1}{N!} \sum_P \langle \mathbf{R} | e^{-\beta H} | P \mathbf{R}' \rangle, \quad (2)$$

where \mathbf{R} and \mathbf{R}' are two configurations of N bosons. The sum over P is over all permutations of particle labels, and $P \mathbf{R}'$ is one such permutation. Permutations lead directly to the off-diagonal long-range order that produces superfluidity. The partition function Z is found by integrating the diagonal elements of the density matrix

$$Z = \frac{1}{N!} \sum_P \int \rho(\mathbf{R}, P \mathbf{R}, \beta) d^3 R. \quad (3)$$

Evaluating the partition function for interacting systems at very low temperatures is complicated by the fact that the kinetic and potential terms in the exponent of the density matrix cannot be separated, so the form of the density matrix is not known in, for instance, the configuration space representation. We can avoid this problem by inserting $M-1$ intermediate configurations into Eq. (3) to obtain the path-integral formulation of the partition function

$$Z = \frac{1}{N!} \sum_P \int \cdots \int d^3 R_1 \cdots d^3 R_{M-1} d^3 R \times \rho(\mathbf{R}, \mathbf{R}_1; \tau) \rho(\mathbf{R}_1, \mathbf{R}_2; \tau) \cdots \rho(\mathbf{R}_{M-1}, P \mathbf{R}; \tau), \quad (4)$$

where $\tau = \beta/M$. The problem of evaluating the partition function at a low temperature β^{-1} has been replaced by the problem of multiple integrations of density matrices at a higher temperature τ^{-1} . The advantage of this is that the high-temperature density matrices may be approximated. In practice, the integrals appearing in Eq. (4) cannot be directly evaluated for systems of strongly interacting particles. Monte Carlo sampling may be used instead to generate configurations and calculate observables.

Equation (4) lends itself to an interesting visualization. The N quantum particles can be thought of as N interacting classical ring polymers, each with M beads. Sampling the partition function then corresponds to sampling the possible configurations of these polymers. Furthermore, particle permutations may be introduced into the Monte Carlo method by splicing together two or more polymer chains. This is known as the polymer isomorphism.

B. Approximating the density matrix

In order to use Monte Carlo sampling on the partition function, we must first provide a starting approximation for the high-temperature density matrices that appear in the integrand of Eq. (4). The simplest starting approximation is to use a very large M , which allows us to separate the density matrix into kinetic and potential energy terms. This is the semiclassical approximation and is exact in the limit $M \rightarrow \infty$, according to the Trotter theorem. For superfluid helium systems it is necessary to go beyond the semiclassical approximation so that the starting temperature may be made as

low as possible. This makes sampling the permutations feasible and speeds the equilibration of the ring polymers by avoiding excessively long chains. The high-temperature density matrix we introduce below can be used with starting temperatures as low as 40 K. We thus only have to use, for instance, $M=40$ to simulate a system at 1 K.

We approximate the high temperature density matrix as a product of the exact free particle solution, an effective two-body interaction found from the exact solution for two interacting helium atoms, and an effective external interaction found from the exact solution for a single atom in a graphite potential:

$$\begin{aligned} \rho(\mathbf{R}, \mathbf{R}'; \tau) &\approx \prod_{i=1}^N \rho_1^{\text{free}}(\mathbf{r}_i, \mathbf{r}'_i; \tau) \\ &\times \prod_{i=1}^N \tilde{\rho}_1^{\text{Gr}}(\mathbf{r}_i, \mathbf{r}'_i; \tau) \\ &\times \prod_{i < j}^N \tilde{\rho}_2^{\text{He}}(\mathbf{r}_{ij}, \mathbf{r}'_{ij}; \tau), \end{aligned} \quad (5)$$

where $\mathbf{r}_{ij} = \mathbf{r}_i - \mathbf{r}_j$. The terms ρ_1^{free} , $\tilde{\rho}_2^{\text{He}}$, and $\tilde{\rho}_1^{\text{Gr}}$ will be discussed below. This approximation assumes that three-body contributions are negligible and that the helium-helium and helium-graphite interactions can be decoupled. The former has been shown to be valid for bulk helium systems with starting temperatures as low as 40 K.

The term ρ_1^{free} is the density matrix for a free particle of mass m , given by

$$\rho_1^{\text{free}}(\mathbf{r}, \mathbf{r}'; \tau) = \lambda_i^{-3} \exp[-\pi(\mathbf{r} - \mathbf{r}')^2 / \lambda_i^2], \quad (6)$$

where $\lambda_i = \sqrt{2\pi\tau\hbar^2/m}$ is the mean thermal wavelength for the temperature $1/\tau$. The helium-helium term $\tilde{\rho}_2^{\text{He}}$ is the interacting part of the solution to the density matrix for two helium atoms. This can be found by separating the density matrix into center-of-mass and relative components. The density matrix for the relative coordinates is a solution to

$$\frac{\partial \rho^{\text{He}}}{\partial \tau}(\mathbf{r}_{ij}, \mathbf{r}'_{ij}; \tau) = [(\hbar^2/m)\nabla^2 - V^{\text{He}}(\mathbf{r}_{ij})] \rho^{\text{He}}(\mathbf{r}_{ij}, \mathbf{r}'_{ij}; \tau). \quad (7)$$

This equation is equivalent to that satisfied by the time evolution propagator in imaginary time. We solve this equation using the methods discussed by Ceperley.²⁹ Briefly, the density matrix can be expanded in a series of partial waves and the expansion coefficients are found by using the matrix-squaring method. The resulting solution is used to define the effective helium-helium interaction $U^{\text{He}}(\mathbf{r}_{ij}, \mathbf{r}'_{ij}; \tau) \equiv -\ln(\tilde{\rho}_2^{\text{He}})$ where $\tilde{\rho}_2^{\text{He}} = \rho^{\text{He}}/\rho^{\text{free}}$. This is a six-dimensional function, but the spherical symmetry of the density matrix allows us to approximate it as a series of one-dimensional functions. This greatly reduces the memory requirements and increases the speed at which the density matrix can be evaluated for a particular configuration.

The density matrix for a single helium atom above a graphite substrate is a solution to

$$\frac{\partial \rho_1^{\text{Gr}}}{\partial \tau}(\mathbf{r}, \mathbf{r}'; \tau) = [(\hbar^2/2m)\nabla^2 - V^{\text{Gr}}(\mathbf{r})]\rho_1^{\text{Gr}}(\mathbf{r}, \mathbf{r}'; \tau), \quad (8)$$

where $V^{\text{Gr}}(\mathbf{r})$ is the full graphite potential. The helium-graphite term $\tilde{\rho}_1^{\text{Gr}}$ is the interacting part of the solution to this equation. Near the substrate, the potential V^{Gr} is anisotropic. A straight forward solution to Eq. (8) is to solve it at grid points within a graphite unit cell using, for instance, a three-dimensional implicit method with periodic boundary conditions at the edges of the cell. The resulting six-dimensional function can be approximated as a series, expanding around the diagonal elements, but this still gives a series of three-dimensional functions. This greatly complicates Monte Carlo simulations of the first-layer atoms using Eq. (5), since storage requirements become large and evaluating the density matrix by interpolating from three-dimensional tables becomes excessively burdensome. Thus, simulating the first adsorbed layer using a high-temperature density matrix is a much more complicated problem than simulating bulk helium. One could always avoid these problems by simply starting at a high enough temperature so that the semiclassical approximation²¹ can be used for atoms near the substrate, but then getting permutations accepted becomes exceedingly unlikely.

The problem becomes much simpler further above the substrate, where corrugations may be ignored. The helium-graphite potential can be found by laterally averaging over the surface, eliminating the x - y plane periodicity that complicates the solution near the substrate. The helium atom experiences only a z -dependent potential, so Eq. (8) can be solved by separating $\rho_1^{\text{Gr}}(\mathbf{r}, \mathbf{r}'; \tau)$ into x , y and z components. The x and y components are one-dimensional, free-particle density matrices. The solution for $\rho(x, x'; \tau)$, for instance, is

$$\rho^{\text{free}}(x, x'; \tau) = \lambda_l^{-1} \exp[-\pi(x-x')^2/\lambda_l^2]. \quad (9)$$

A similar solution exists for $\rho(y, y'; \tau)$. The z dependence is found by solving the parabolic partial differential equation

$$\frac{\partial \rho}{\partial \tau}(z, z'; \tau) = [(\hbar^2/2m)\partial^2/\partial z^2 - V^{\text{Gr}}(z)]\rho(z, z'; \tau), \quad (10)$$

where $V^{\text{Gr}}(z)$ is the laterally averaged potential.³⁶ This can be solved by matrix squaring, or by an implicit method.³⁷ The initial condition is that the density matrix is a delta function at $\tau=0$. We define the effective interaction for the helium-graphite density matrix, $U^{\text{Gr}}(z, z'; \tau) \equiv -\ln[\rho(z, z'; \tau)/\rho^{\text{free}}(z, z'; \tau)]$. This is still a function of two variables. In order to make evaluating the density matrix efficient during the Monte Carlo runs, we expand U^{Gr} as a series of one dimensional functions. We rewrite $U^{\text{Gr}}(z, z') = U(\bar{z}, \Delta z)$, where $\bar{z} = (z+z')/2$ and $\Delta z = |z-z'|$. The matrix is dominated by the diagonal elements, so we expand it as a series about $(\Delta z)^2$:

$$U^{\text{Gr}}(z, z'; \tau) = \frac{U^{\text{Gr}}(z, z; \tau) + U^{\text{Gr}}(z', z'; \tau)}{2} + \sum_m U_m(\bar{z})(\Delta z)^{2m}. \quad (11)$$

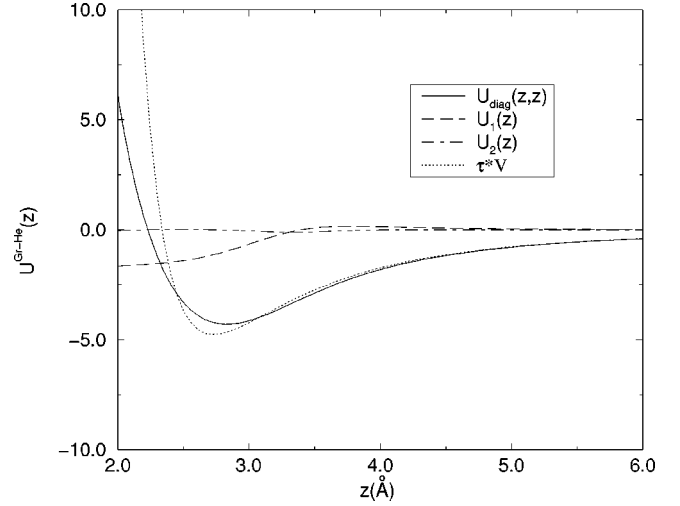


FIG. 1. The diagonal and lowest-order off-diagonal terms of the expansion of U^{Gr} , Eq. (11). The semiclassical approximation is also shown. The laterally averaged potential was used and $\tau = 0.025 \text{ K}^{-1}$.

The average over the two diagonal parts of the solution in the first term is called the end-point approximation. The functions $U_m(\bar{z})$ are found by χ^2 fitting Eq. (11) to the exact solution. One simply terminates the series when the approximation is sufficiently close to the exact solution. Results for the diagonal solution and the first two expansion terms are shown in Fig. 1. The off-diagonal terms become negligible for $z > 4 \text{ \AA}$. The diagonal solution can be compared with the semiclassical approximation. Figure 2 compares the exact solution for off-diagonal elements to the expansion, Eq. (11), and the end-point approximation, $1/2[\tau V(z) + \tau V(z')]$.

C. Sampling the density matrix

With the first layer frozen, the density matrix, Eq. (5), for the active second layer atoms can be written in the form $\rho = \exp(-S)$, where

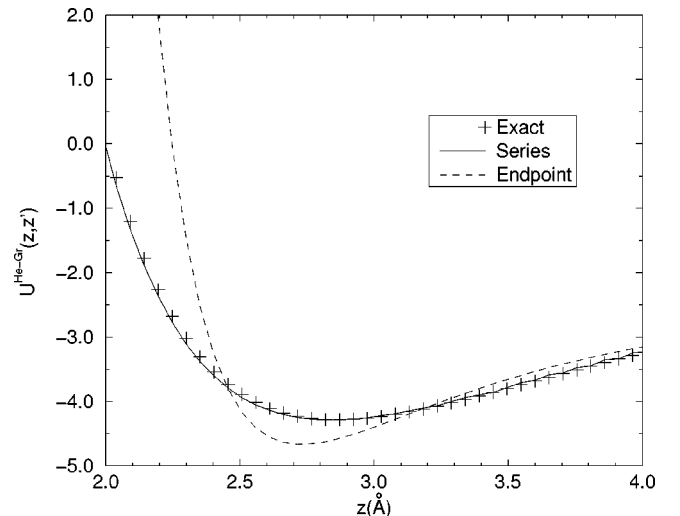


FIG. 2. The exact solution $U^{\text{Gr}}(z, z'; \tau)$ for $z' = 2.82 \text{ \AA}$ compared with the expansion Eq. (11) and the end-point approximation using τV .

$$\begin{aligned}
S(\mathbf{R}, \mathbf{R}'; \tau) = & (3N_{\text{act}}/2) \ln(\lambda_i^2) + \frac{\pi(\mathbf{R} - \mathbf{R}')^2}{\lambda_i^2} \\
& + \frac{1}{2} \sum_{i=1}^{N_{\text{act}}} \sum_{j=1}^{N_{\text{act}}} U^{\text{He}}(\mathbf{r}_{ij}, \mathbf{r}'_{ij}; \tau) \\
& + \sum_{i=1}^{N_{\text{act}}} \sum_{j=1}^{N_{\text{fr}}} U^{\text{He}}(\mathbf{r}_{ij}, \mathbf{r}'_{ij}; \tau) + \sum_{i=1}^{N_{\text{act}}} U^{\text{Gr}}(z_i, z'_i; \tau),
\end{aligned} \tag{12}$$

where $r_{ij} = |\mathbf{r}_i - \mathbf{r}_j|$. The number of active and frozen helium atoms is given by N_{act} and N_{fr} , respectively. In the polymer isomorphism, S is the action for a system of interacting polymers. In sampling the paths, we are effectively choosing between two different polymer configurations. The one with the lower action is the more favorable configuration, and is more likely to be chosen in a Metropolis-style acceptance test.

As in standard Monte Carlo simulations, the interaction U^{He} is cut off at some maximum distance $r_c \leq \min(L_x, L_y)$, where L_x and L_y are the dimensions of the simulation cell. The long-range correction to the interaction felt by each particle is, in cylindrical coordinates (ρ, z) ,

$$U_{LR}^{\text{He}} = 2\pi \int_0^\infty n(z') dz' \int_{\rho_c}^\infty \rho d\rho U^{\text{He}}(r, r; \tau), \tag{13}$$

where $r = \sqrt{\rho^2 + (z - z')^2}$, $\rho_c^2 = r_c^2 - (z - z')^2$, and only diagonal elements need to be considered. The integral of $n(z')$ gives the density of the system. We make the approximation that the layer thicknesses can be treated as delta functions. This is exact for the frozen first layer. Then $n(z') = n_{\text{fr}} \delta(z' - z_{\text{fr}}) + n_{\text{act}} \delta(z' - z_{\text{act}})$ and

$$U_{LR}^{\text{He}} = 2\pi \int_{\rho_c}^\infty \rho d\rho [n_{\text{fr}} U^{\text{He}}(r, r; \tau) + 1/2 n_{\text{act}} U^{\text{He}}(r, r; \tau)], \tag{14}$$

where n_{fr} and n_{act} are the densities of the first (frozen) and second (active) layers. The factor of one-half before the contribution from the active layer is needed to avoid double counting. A similar long-range correction is added to $\partial U^{\text{He}}/\partial \tau$ in the energy calculation.

As we have emphasized, particle permutations must be included in simulations of superfluid helium. These permutations correspond to splicing together two or more of the polymer rings. This splicing can be accomplished by proposing cyclic permutations involving one to four particle labels on inverse-temperature slice $i+n$ relative to slice i , where $n = 2^l$ and l is the overall level of the move. The paths followed by the permuted particles on the intermediate slices $i+1$ to $i+n-1$ that produce the permutation are then filled in by successively bisecting the interval i to $i+n$. This is known as multilevel Monte Carlo sampling, an extension of the standard Metropolis method. The interested reader is referred to a recent review article on the subject.²⁹

In our Monte Carlo runs for helium films, we take $l=3$, since this gives the best balance between accepting single particle and multiple particle moves. Increasing l increases the number of permutations that can be accepted but de-

creases the overall acceptance rate, while decreasing l has the opposite effect. The overall acceptance rate for the moves varies between 8% and 15%, depending on the density. Tests using $l=2$ at selected densities showed that the $l=3$ results had converged. The acceptance rate of multiparticle permutations is small, between 0.2 and 0.3% in the liquid phase. We have found that similar small acceptance rates are sufficient to obtain the superfluid density in bulk simulations.

D. Calculating observables

The expectation value of an observable, A , can be found from the trace $\langle A \rangle = Z^{-1} \text{Tr} A \rho$. We use PIMC to calculate expectation values for the total energy, the superfluid density, and the static structure factor. Below we give formulas for each of these calculations for a helium film on a substrate.

The total energy is given by the expectation value

$$E = \frac{3N_{\text{act}}}{2\tau} + \left\langle -\frac{\pi(\Delta \mathbf{R})^2}{\lambda_i^2 \tau} + \frac{dU_{\text{total}}^{\text{He}}}{d\tau} + \frac{dU_{\text{total}}^{\text{Gr}}}{d\tau} \right\rangle. \tag{15}$$

$\Delta \mathbf{R}$ is the change in the particle positions between two consecutive inverse-temperature slices. The terms $U_{\text{total}}^{\text{He}}$ and $U_{\text{total}}^{\text{Gr}}$ are shorthand for the sums over the interaction terms in Eq. (12). Notice that the zero of the total energy occurs at zero second-layer coverage, where there are no active atoms.

The superfluid density can be calculated using the winding number \mathbf{W} for simulations that have periodic boundary conditions. Nonzero winding numbers occur when particles, through a series of permutations, are permuted with periodic images of themselves. The winding number is directly related to ρ_s , the superfluid density.²⁹ For a system with periodic boundary conditions in the x - y plane, the superfluid density is given by

$$\frac{\rho_s}{\rho} = \frac{m \langle (\mathbf{W} \cdot \mathbf{L})^2 \rangle}{2\beta \hbar^2 N_{\text{act}}}, \tag{16}$$

where the elements L_x and L_y are the dimensions of the simulation cell.

Finally, structural information can be obtained with the static structure factor

$$S(\mathbf{k}) = \frac{1}{N_{\text{act}}} \langle \rho(\mathbf{k}) \rho(-\mathbf{k}) \rangle. \tag{17}$$

We take $\hat{\mathbf{z}}$ to be perpendicular to the plane of the substrate, so $\mathbf{k} = (k_x, k_y)$. $\rho(\mathbf{k}) = \sum_{i=1}^{N_{\text{act}}} \exp(i\mathbf{k} \cdot \mathbf{r}_i)$ is the Fourier transform of the density.

E. Testing the method

As can be seen from the previous discussion, simulating helium systems below the superfluid transition is an extremely complicated task, and it is important to verify all parts of the method. We have verified our calculations for the solution to Eq. (7) by comparing our results to published results for the Lennard-Jones³⁸ potential and to the Aziz potential. The solution to Eq. (10) for the helium-graphite density matrix was checked by comparing the results obtained from the matrix squaring and implicit solution methods. We

have verified that the full Monte Carlo method outlined above works for bulk helium systems by reproducing reported values for the energy, specific heat, and superfluid density.^{33,35} We believe these tests sufficiently prove that our simulation method works and can be extended to helium films.

F. Choosing simulation cells

We perform calculations with a variety of simulation cells that are appropriate for examining different regions of the second-layer phase diagram. The first consideration is to choose a simulation cell that will match the periodicity of the first-layer triangular solid. This can be done by using a rectangular unit cell with a two-point basis, with unit vectors $\mathbf{a}_1 = a\hat{x}$ and $\mathbf{a}_2 = \sqrt{3}a\hat{y}$, where $a = 3.015 \text{ \AA}$. Two first-layer helium atoms are located in each unit cell at $\mathbf{b}_1 = 0$ and $\mathbf{b}_2 = \mathbf{a}_1/2 + \mathbf{a}_2/2$. This gives a coverage of $0.1270 \text{ atom/\AA}^2$, the fully compressed first-layer density.⁵ In examining the second layer, our first goal is to scan the layer at intermediate and higher densities by varying the number of particles and to calculate the total energy at each density. For these calculations we use simulation cells with dimensions $(5\mathbf{a}_1, 3\mathbf{a}_2)$ and $(8\mathbf{a}_1, 5\mathbf{a}_2)$, hereafter referred to as the 5×3 cell and the 8×5 cell, respectively. The number of active particles in calculations using the 5×3 cell ranged from 8 to 21, corresponding to densities 0.1605 to $0.2159 \text{ atom/\AA}^2$. Calculations with the 8×5 cell had 24 to 52 active particles, corresponding to densities between 0.1651 and $0.2096 \text{ atom/\AA}^2$. These two simulation cells are nearly square, which is useful for calculating winding numbers. As will be discussed in Sec. III, the energy calculations for the 5×3 cell are used to verify that finite-size effects are not important in the 8×5 cell. Our conclusions about the coverage ranges of various phases are drawn from results using the 8×5 cell.

At high second-layer densities, commensurate and incommensurate triangular solid phases occur. In order to further investigate these phases, we use simulation cells that can contain an integer number of unit cells of both the first- and second-layer solids. That is, the simulation cells have the periodicity of both the first- and second-layer solids. It is also important to note that the solid phases will tend to align with the x and y axes of the simulation cell. For the incommensurate solid we use a cell with dimensions $(5\mathbf{a}_1, 5\mathbf{a}_2)$, hereafter referred to as the 5×5 cell. This cell can accommodate 32 second layer atoms in an equilateral triangular lattice. A diagram of a second-layer incommensurate solid in the 5×5 cell is shown in Fig. 3. The second-layer solid is incommensurate with respect to the first since no supercell with dimensions less than the minimum dimension of the simulation box can be drawn in which both first- and second-layer atoms are periodically repeated.

The simulation of the $\sqrt{7} \times \sqrt{7}$ triangular commensurate solid presents an additional problem since this structure is rotated with respect to the first layer. This triangular solid can be regarded as having a rectangular unit cell with a fourteen point basis. The unit vectors for this solid are $\mathbf{s}_1 = 2\mathbf{a}_1 + \mathbf{b}_2$ and $\mathbf{s}_2 = -2\mathbf{a}_1 + \mathbf{a}_2 + \mathbf{b}_2$. Note that $|\mathbf{s}_2| = \sqrt{3}|\mathbf{s}_1|$ and $|\mathbf{s}_i| = \sqrt{7}|\mathbf{a}_i|, i = 1, 2$. We use simulation cells with dimensions $(2\mathbf{s}_1, 2\mathbf{s}_2)$ and $(3\mathbf{s}_1, 2\mathbf{s}_2)$ to identify the solid configuration and calculate the static structure factor. The commensurate

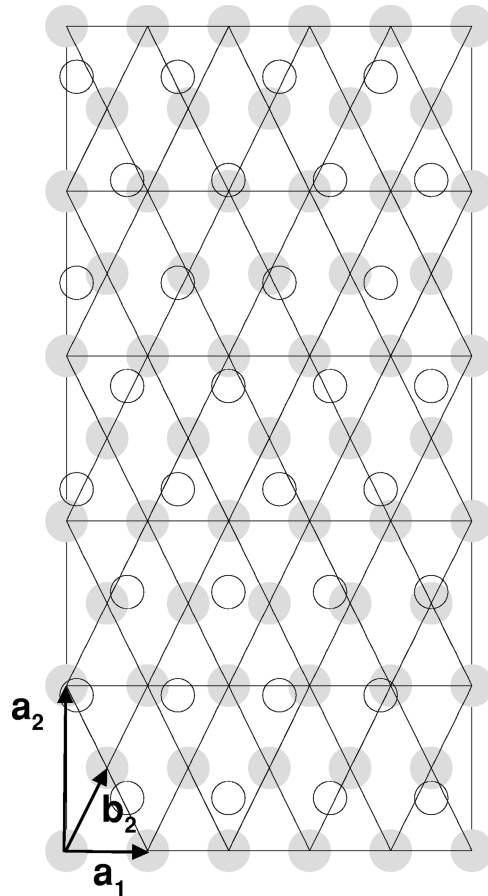


FIG. 3. Diagram of the 5×5 simulation cell. The shaded circles denote positions of the first layer atoms. The 32 open circles denote possible positions of atoms in the second-layer incommensurate triangular solid. The arrows indicate the unit vectors for the solid described in the text. The lines emphasize the triangular structure of the solid.

density $0.1996 \text{ atom/\AA}^2$ corresponds to 32 and 48 active particles, respectively, for these two cells.

A diagram of the $(3\mathbf{s}_1, 2\mathbf{s}_2)$ simulation cell with the second layer atoms in $\sqrt{7} \times \sqrt{7}$ registry is shown in Fig. 4. The large, rotated rectangle gives the bounds of the simulation cell. First layer atom positions outside this rectangle are periodic images of interior atoms. Note that the location of the origin is arbitrary. It is not necessary, for instance, to place it at a high symmetry point of the first-layer lattice, such as over a first-layer atom or at a potential minimum. The essential requirements for the existence of the partially registered solid are that once the origin is chosen, all of the two-dimensional space can be divided up into periodically repeated superlattice unit cells (supercells), and that the relationships of the first- and second-layer atoms to each other and to the supercell are the same in every supercell. We have chosen the origin so that the second-layer atoms can be used to divide up the rectangle into supercells. These (primitive) supercells are the equilateral parallelograms formed by the heavily shaded lines in the interior of Fig. 4. They can be seen to exactly fill the rectangle. Second layer atoms are located at the four corners, on each of the four sides at the midpoints between the corners, and at the center of each supercell, so there is a four-point basis of second-layer atoms

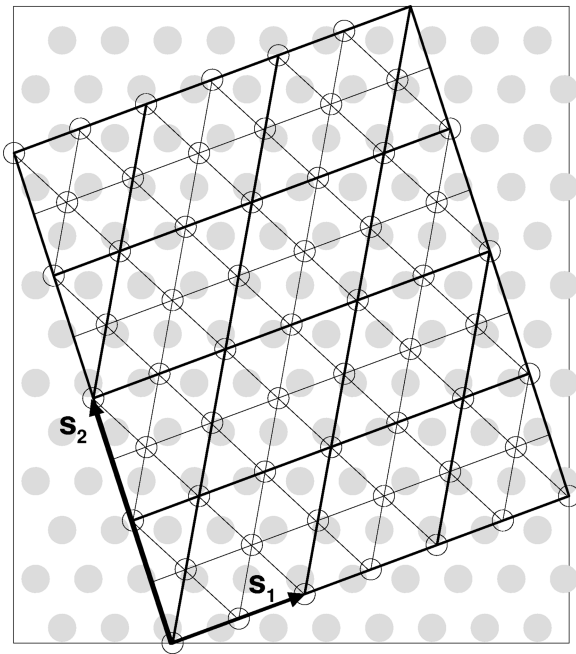


FIG. 4. Diagram of a simulation cell used for the $\sqrt{7} \times \sqrt{7}$ solid. The dimensions are $(3s_1, 2s_2)$. The shaded circles denote positions of the first layer triangular solid. The open circles denote possible positions of the second layer registered solid. The arrows indicate the unit vectors for the solid described in the text. The lines emphasize the triangular structure of the solid. The heavily shaded lines indicate the $\sqrt{7} \times \sqrt{7}$ supercells.

in each cell. The positions of the first-layer atoms can also be seen to be periodically repeated in every supercell.

III. RESULTS

A. Identification of phases

Experimentally, there is evidence for liquid, commensurate solid, and incommensurate solid phases in the second layer. We now describe the identification of all three phases in our simulation.

To find the liquid phase, we are guided first by the torsional oscillator measurements, which detect a liquid phase between 0.174 and 0.187 $\text{atom}/\text{\AA}^2$. We also find evidence that densities in this range are liquid in our simulation. Figure 5 shows a snapshot of a typical liquid density. The second-layer atoms obviously do not possess spatial ordering, and the configuration covers the entire surface. More direct evidence that the system has a liquid phase comes from that static structure factor. Figure 6 shows the result of a calculation, which is typical of a self-bound liquid, at the coverage 0.1860 $\text{atom}/\text{\AA}^2$.

Commensurate and incommensurate solid phases can be identified by a similar procedure. A particularly nice feature of PIMC is that these solids form on their own, without any modifications to the high-temperature density matrix, Eq. (5). In contrast, previous variational calculations have used different trial wave functions for the liquid and solid phases.¹⁹ This can be avoided by using a shadow wave function, but such calculations have not been performed for two-dimensional helium or helium films.

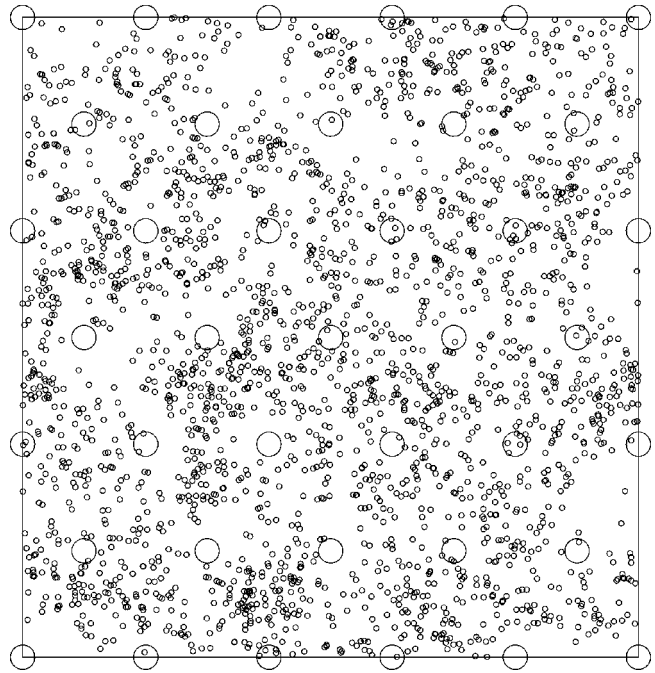


FIG. 5. Snapshot of a liquid configuration at 0.1778 $\text{atom}/\text{\AA}^2$, found using the 5×3 simulation cell with twelve active particles and $T=200$ mK. Large circles indicate frozen first-layer atom sites. The instantaneous configuration of the second-layer atoms is indicated by the small circles.

As demonstrated previously,¹³ we have observed the $\sqrt{7} \times \sqrt{7}$ commensurate solid phase in our simulation for temperatures below 1 K. The structure of this phase was determined by examining snapshots of the configurations generated by the simulation. Particle paths of the second layer atoms were observed to localize around the $\sqrt{7} \times \sqrt{7}$ lattice sites shown in Fig. 4. We note further that we do not bias the simulation of this solid by beginning the configuration at the commensurate lattice sites. The existence of the incommensurate solid, which occurs at a higher density than the commensurate phase, has also been demonstrated. A snapshot of

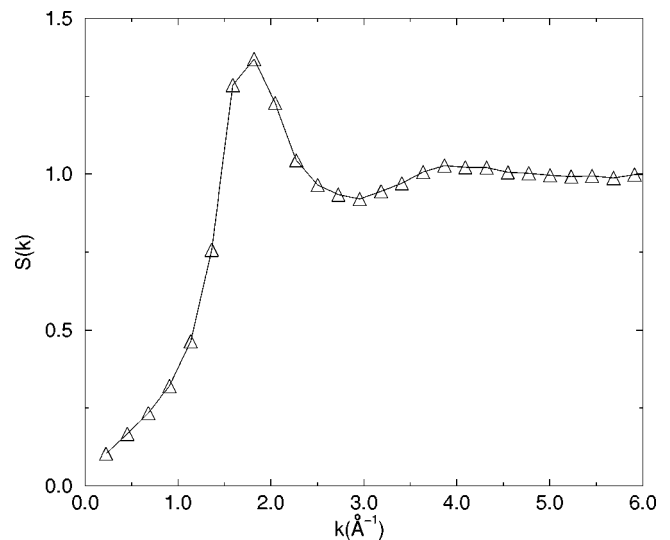


FIG. 6. The static structure function for the liquid phase at the density 0.1860 $\text{atom}/\text{\AA}^2$ and $T=500$ mK with 26 particles.

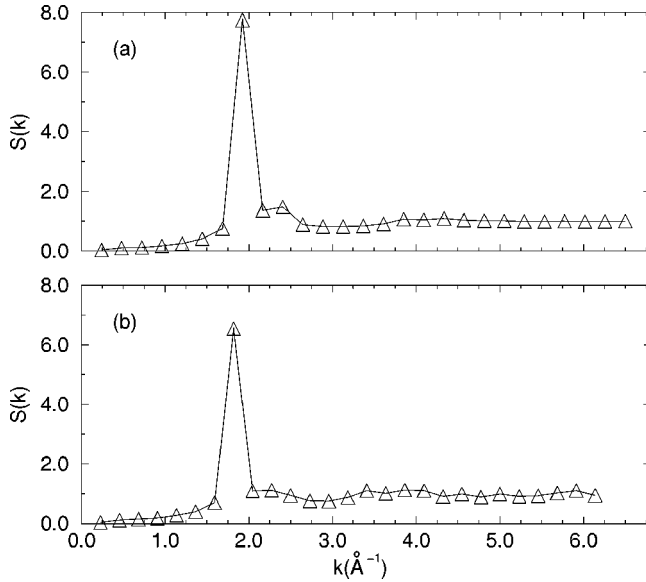


FIG. 7. The static structure factor calculated in the (01) direction for (a) the incommensurate solid at $0.2083 \text{ atom/\AA}^2$ and 0.67 K with 32 particles, and (b) the commensurate solid at $0.1996 \text{ atom/\AA}^2$ and 0.50 K with 32 particles. The errors are the size of the symbols.

this configuration generated by our simulation can be found in our previous publication.¹³ This phase matches the diagram shown in Fig. 3. We identify this phase as incommensurate because no supercell with dimensions less than the minimum simulation box dimension can be drawn that has both first- and second-layer atoms periodically repeated, in contrast to the commensurate phase.

The snapshots of the two solids are useful for visualizing their structure but are not actual tests for their existence. A direct measurement of correlation comes from the static structure factor. Results for these calculations in the (01) reciprocal lattice direction for the incommensurate and commensurate phases are shown Figs. 7(a) and 7(b). The structure factor is normalized to N_{act} . The locations of these peaks give the correct lattice spacings for the diagrams shown in the Figs. 3 and 4. The peak for the commensurate solid occurs at 1.82 \AA^{-1} , which gives the correct lattice constant, 3.99 \AA , for the $\sqrt{7} \times \sqrt{7}$ triangular solid. Likewise, the peak for the incommensurate solid occurs at 1.93 \AA^{-1} , corresponding to a lattice constant of 3.76 \AA , which is the correct lattice spacing for a triangular solid at $0.2083 \text{ atom/\AA}^2$.

B. $T=0$ phase diagram

Having identified the liquid, commensurate solid, and incommensurate solid phases of the second layer, we now wish to find the boundaries for each of the phases. We are able to identify the following density regions at low temperature. At low second-layer coverages, 0.1270 to $0.1750 \text{ atom/\AA}^2$, the system is in a gas-liquid coexistence region, which consists of a liquid droplet and a zero density gas. The equilibrium density for the liquid is $0.1750 \text{ atom/\AA}^2$, and the layer is uniformly covered by a liquid phase from 0.1750 to $0.1905 \text{ atom/\AA}^2$. Above this density, the liquid coexists with the $\sqrt{7} \times \sqrt{7}$ commensurate solid phase discussed in the

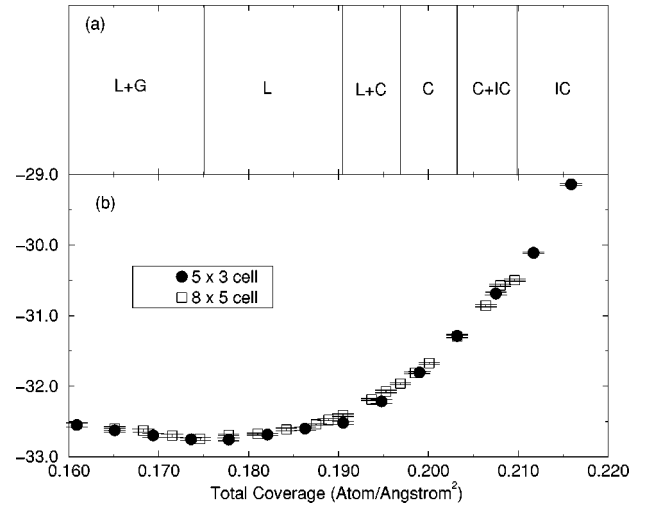


FIG. 8. (a) Summary of phase boundaries determined from applying the Maxwell construction to the total energy of the 8×5 cell. The phases are liquid-gas (L+G), liquid (L), liquid-commensurate solid (L+C), commensurate solid (C), commensurate solid-incommensurate solid (C+IC), and incommensurate solid (IC). (b) The energy per particle for the 5×3 (circles) and 8×5 (squares) cells.

previous section. This LC coexistence occurs from 0.1905 to $0.1970 \text{ atom/\AA}^2$, and is followed by the commensurate phase between 0.1970 and $0.2032 \text{ atom/\AA}^2$. The incommensurate solid phase begins to form above $0.2032 \text{ atom/\AA}^2$ and there is CIC coexistence until $0.2096 \text{ atom/\AA}^2$. Above this density, until layer promotion to the third layer at 0.212 atom/\AA^2 , the system is completely in the incommensurate phase. These results are summarized in Fig. 8(a).

Before discussing how these ranges were determined, we would first like to demonstrate that finite-size effects play an unimportant role in the energy values used in the Maxwell construction. Figure 8(b) shows the energy per particle found using the 8×5 and 5×3 cells. Almost all of the points calculated at similar densities in the two cells are consistent. The primary ‘‘size effect’’ is the limitation on the available densities which may be examined for a given simulation cell.

Phase ranges are determined by using the Maxwell double-tangent construction, which identifies unstable regions associated with the coexistence of two phases. A coexistence region at zero temperature in the thermodynamic limit will have a total ground state energy that is the weighted average of the two constituent phases’ energy values. In Monte Carlo simulations the energy in the coexistence region will lie above the coexistence line, either because the system remains in an unphysical homogeneous state or because creating the phase boundary has a finite energy cost.³⁹ We may thus identify a coexistence region as the maximum range of densities in which all the intermediate energy values lie on or above a line connecting the values at the end points. We note that this version of the Maxwell construction is somewhat different from other applications,^{19,25,20} which apply the Maxwell construction to the free energy dependence on atomic area (inverse density). Our method is appropriate for simulations with constant area and varying particle number.

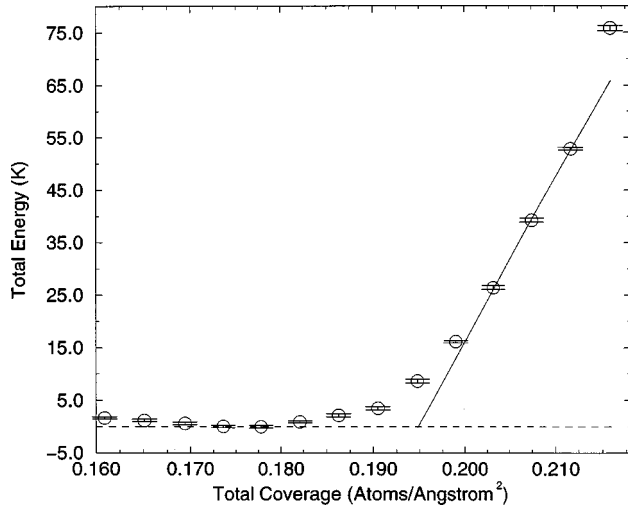


FIG. 9. The total energy found using the 5×3 simulation cell with $N_{\text{act}}=8,9,\dots,21$ and $T=200$ mK. The dashed line is gas-liquid coexistence line. The solid line indicates a coexistence region terminating in an incommensurate solid phase.

At finite temperatures, the Maxwell construction should be applied to the total free energy. Unfortunately, the free energy is not directly accessible from the PIMC simulation. We instead make use of the fact that at very low temperatures the free energy and the energy are approximately the same, and become identical at zero temperature. We can thus apply the Maxwell construction to low temperature energy values to determine an effectively zero-temperature phase diagram, provided that the values have converged to their zero-temperature limits. To implement this procedure, we first calculated energy values for a range of second-layer densities at 200 mK. Selected energy values were recalculated at a higher temperature, typically 400 mK, and were seen to be within error bars of the 200 mK results. This indicates that our 200 mK calculations are effectively zero-temperature results.

The application of the Maxwell construction to the total energy values calculated using the 8×5 box has been shown in our previous publication.¹³ Figure 8(a) summarizes the results. The energy minimum was determined to occur at $0.1746 \text{ atom}/\text{\AA}^2$ (30 particles). For comparison, Fig. 9 shows the energy calculations using the 5×3 cell. These energy values have been shifted by $N_{\text{act}}e_{\text{min}}$ for clarity, where $e_{\text{min}} = -32.754 \pm 0.020$ K. The energy minimum occurs at $0.1778 \text{ atom}/\text{\AA}^2$ (12 particles). Note that for both simulation cells the minimum energy per particle occurs at nearly the same coverage value, despite the fact that the 8×5 cell is $2 \frac{2}{3}$ times as large as the 5×3 cell. In general, we find all the energy values calculated with the two cells to be in agreement. See Fig. 8(b).

The low density region of the second layer is known experimentally to have coexistence between a gas phase and a superfluid liquid phase. In order to determine the gas-liquid coverage range in our simulation, we take the gas phase to have zero density at zero temperature and thus zero total energy. Two-dimensional calculations²⁰ confirm that this assumption is correct for low temperatures. A coexistence line can then be drawn between the beginning of the second layer, $0.1270 \text{ atom}/\text{\AA}^2$, and the density with the minimum

energy per particle, which occurs between 0.174 and $0.178 \text{ atom}/\text{\AA}^2$ in the 8×5 cell. The best χ^2 parabolic fit to the energy data around the minimum gives $\rho_0 = 0.1750(6) \text{ atom}/\text{\AA}^2$ for the density of minimum energy. The number in parenthesis is the error in the last digit. A similar coexistence line can be identified in the 5×3 cell, Fig. 9. We find that $\rho_0 = 0.1752(6)$, so finite-size effects on the liquid density are small. At sufficiently low temperatures, this liquid phase will become superfluid, as will be discussed below. All measured energy values for the densities between $0.1270 \text{ atom}/\text{\AA}^2$ and ρ_0 lie above the coexistence line, so the system is in gas-liquid coexistence for this density range.

The density of uniform liquid coverage ρ_0 can be compared to experimental results. For $T \leq 0.2$ K the second-layer heat capacity measurements⁴ show a probable gas-liquid region roughly between 0.13 and $0.16 \text{ atom}/\text{\AA}^2$. Within the resolution available from the data, this phase can terminate anywhere from $0.1600 \text{ atom}/\text{\AA}^2$ up to, but not including, $0.1700 \text{ atom}/\text{\AA}^2$ total coverage. Since the first-layer coverage in the experiment is between 0.120 and 0.127 for these densities, gas-liquid coexistence terminates at second-layer coverages anywhere from 0.033 to $0.050 \text{ atom}/\text{\AA}^2$. For comparison, the gas-liquid phase terminates at the second layer coverage $0.0480(6) \text{ atom}/\text{\AA}^2$ in our simulation. Superfluidity is first observed in the torsional oscillator measurements at $0.174 \text{ atom}/\text{\AA}^2$. Thus, the superfluid signal, as observed by this technique, becomes significant at the coverage where our simulation determines that the second layer is uniformly covered by the liquid phase.

The density we determine for uniform liquid coverage can also be compared to other simulations. In the two-dimensional calculations of Whitlock *et al.*, the equilibrium liquid coverage is $0.04356 \text{ atom}/\text{\AA}^2$ at zero temperature. This result is supported by the low-temperature results of 2D PIMC calculations.²⁰ This is slightly below our onset coverage, perhaps because we allow for particle motion perpendicular to the substrate. Other calculations for helium films also show a slight increase in the equilibrium density relative to the 2D result. In the Monte Carlo calculation for the first layer of helium on graphite,²² the equilibrium density is determined to be $0.0443 \text{ atom}/\text{\AA}^2$. The effects of wave function spreading will be even greater in the second helium layer. Wagner and Ceperley's simulation of helium adsorbed on solid hydrogen²⁶ also demonstrated that the liquid equilibrium density increases when motion perpendicular to the substrate is allowed. They find a liquid coverage of $0.046(1) \text{ atom}/\text{\AA}^2$, comparable to our result. Thus the calculations of films with perpendicular spreading show a trend toward higher liquid densities, with the onset density approaching the 2D value as the helium-substrate potential becomes stronger. From a 2D viewpoint, this can be understood as a reduction of the hardcore repulsion, which allows for closer crowding.

At the highest second-layer densities, we can identify another unstable region in the total energy values of the 8×5 cell between 0.2032 and $0.2096 \text{ atom}/\text{\AA}^2$, corresponding to the CIC mixed phase. As shown previously,¹³ the coexistence line can be drawn between the total energy values at these two densities. The intermediate energy values lie on or above this line, so the region has coexisting phases. In particular, the energy value at $0.2080 \text{ atom}/\text{\AA}^2$ was found to lie

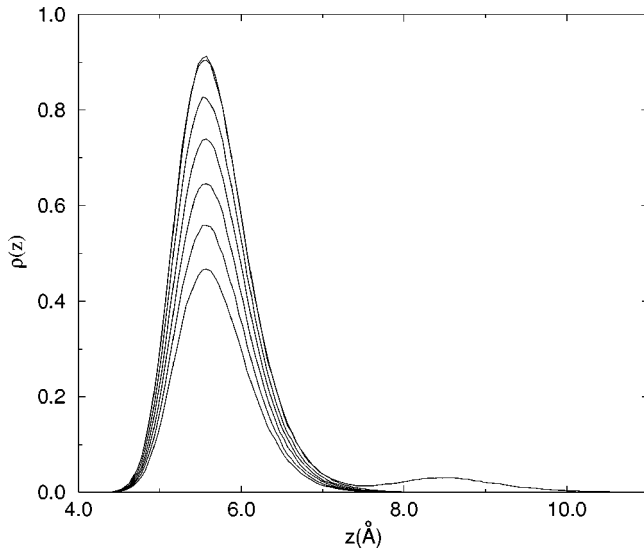


FIG. 10. Density profiles for the second layer found using the 5×3 cell, with densities 0.1694, 0.1778, 0.1863, 0.1948, 0.2032, 0.2117, and 0.2159 $\text{atom}/\text{\AA}^2$.

completely above the coexistence line, providing an unambiguous signal for coexistence. The range we find is in good agreement with the coexistence region 0.2030 to 0.2080 $\text{atom}/\text{\AA}^2$ that can be determined from the heat capacity peaks.⁵ This phase coexistence is not a product of finite-size effects. The beginning of a similar region may be identified between the densities 0.2032 and 0.2117 $\text{atom}/\text{\AA}^2$ in the 5×3 simulation cell, Fig. 9. Phase coexistence in fact becomes clearer in the 8×5 cell because we are able to examine more density values in the unstable region.

The presence of the C phase at 0.1996 $\text{atom}/\text{\AA}^2$ requires an LC coexistence region between it and the liquid. The region can also be identified in the 8×5 cell. The end points of the LC phase are 0.1905 and 0.1969 $\text{atom}/\text{\AA}^2$. The intermediate energy values lie on the coexistence line within error bars. The LC range is in reasonable agreement with the coexistence range 0.1871 to 0.1970 $\text{atom}/\text{\AA}^2$ determined from heat capacity measurements.⁵ Torsional oscillator measurements¹⁰ also indicate that the coexistence region begins at about 0.187 $\text{atom}/\text{\AA}^2$. The LC phase cannot be determined in the 5×3 cell due to the coarseness of the coverage grid.

C. Other properties

Figure 10 depicts the density profiles for selected layer densities. These plots are normalized such that integrating $\rho(z)$ gives the number of particles. Promotion to the third layer can be clearly observed at the highest density shown, 0.2159 $\text{atom}/\text{\AA}^2$, so we conclude that layer promotion occurs between 0.2117 and 0.2159 $\text{atom}/\text{\AA}^2$. This is in excellent agreement with the completion density of 0.212 $\text{atom}/\text{\AA}^2$ determined from the heat capacity measurements.^{4,5} A somewhat lower value of 0.204 $\text{atom}/\text{\AA}^2$ for third layer promotion is obtained from the isothermal compressibility minima.^{1,11} Also of note, Whitlock *et al.*²² estimate that promotion to the third layer begins at the second-layer coverage of 0.08 $\text{atom}/\text{\AA}^2$, quite close to but somewhat lower than our value of 0.085 $\text{atom}/\text{\AA}^2$.

The temperature dependence of the energy and superfluid density at a sample liquid density of 0.1778 $\text{atom}/\text{\AA}^2$ have been determined. This coverage corresponds to a second-layer coverage of 0.0508 $\text{atom}/\text{\AA}^2$. Values were calculated using the 5×3 simulation cell with twelve active particles, and are illustrated in a previous publication.¹³ The superfluid density is relative to the second-layer density. Both the energy and the superfluid density converge to the ground state for temperatures below 0.8 K. The slow decay of the superfluid density at higher temperatures is a typical 2D finite-size effect.⁴⁰ The superfluid density values have been χ^2 fit to the solution to the Kosterlitz-Thouless (KT) recursion relations.⁴¹ From the intersection of the fit and the KT transition line, we estimate the transition temperature to be $T_c \approx 0.88$ K. For comparison, the 2D PIMC simulation²⁰ obtains $T_c = 0.86 \pm 0.02$ K at 0.0508 $\text{atom}/\text{\AA}^2$.

The specific heat of the liquid, commensurate solid, and incommensurate solid phases can be found by differencing the energy per particle with respect to temperature. This was shown in our previous publication.¹³ For the liquid phase, a broad, low peak with a maximum value at 1.18 K was found. This is comparable to the experimental heat capacity results,⁵ which have a peak at 1 K. For the commensurate solid phase, a specific heat peak at about 1.5 K was found. This is comparable to the heat capacity measurements⁵ at similar density values, which also have a peak at 1.5 K. This close agreement provides some additional evidence that the $\sqrt{7} \times \sqrt{7}$ C phase occurs in the experiment. Finally, for the IC solid, a peak at 0.7 K was obtained, somewhat lower than the peak in the heat capacity measurements at the same density, which occurs at 1 K.

IV. SUMMARY

A number of recent experiments indicate that the second layer of helium on graphite has an interesting phase diagram. Torsional oscillator measurements detect superfluidity over a narrow density range in this layer.^{10,11} Neutron scattering⁷⁻⁹ detects an incommensurate solid phase at high densities. Heat capacity measurements^{4,5} have found evidence for liquid-gas coexistence and the incommensurate solid phase. The heat capacity data also show the existence of an intermediate phase between the liquid and incommensurate solid, which is possibly a commensurate solid. The existence of this commensurate solid phase would explain the disappearance of superfluidity at higher second layer coverages. Motivated by these experiments, we have undertaken a simulation of this layer.

In order to study the second layer with a Monte Carlo simulation for a range of temperatures, it is necessary to develop a method that incorporates both particle permutations and the effects of the substrate and the solid first layer on the second. Permutations are necessary to obtain the superfluid phase. The effects on the solid first layer must be included since the commensurate second layer solid is partially registered with respect to the first layer. First-layer and substrate effects also play a role in the formation of the incommensurate solid phase, which replaces the commensurate phase before layer promotion begins.

We have developed a path-integral Monte Carlo method that includes the above features. Particle permutations were

included in the simulation using a method developed for bulk helium.²⁹ We have shown that the helium-helium and helium-graphite interactions can be incorporated into the simulation by using effective interactions found from the exact solutions for the interacting part of the appropriate density matrices. Realistic helium-helium and helium-graphite potentials are used to find these effective interactions. For the helium-graphite effective interactions, we have shown how this solution may be approximated so that off-diagonal matrix elements may be efficiently and accurately included in Monte Carlo sampling. The interaction of the second layer of helium atoms with the solid first layer was approximated by placing first layer atoms at triangular lattice sites with a lattice spacing that gives the completed first layer density. These atoms were located at a fixed height above the substrate, given by the minimum of the effective helium-graphite interaction. Configurations of these atoms were not sampled, which allowed us to scan second layer densities with a finer grid. Therefore, we study the second layer atoms under the influence of their mutual interactions and a static potential produced by the frozen graphite substrate and the frozen first layer helium atoms. This approach ignores effects on the second layer from the zero point motion of the first layer solid and first layer compression effects. We feel this is a reasonable approximation because the relatively high Debye temperature of the completed first layer³¹ means that it will be relatively stiff for the temperatures of our simulation. Compression effects on the first layer by the second are most important for low second layer densities,¹⁵ below the range of our simulation.

Using the above simulation method, we were able to identify, in order of increasing density, superfluid liquid, $\sqrt{7} \times \sqrt{7}$ commensurate triangular solid, and incommensurate triangular solid phases from particle configurations and static structure factor calculations. We also calculated the specific heat for each of these phases and observed peaks in general agreement with experiment.

The density ranges at effectively zero temperature of each of the second layer phases and their coexistence regions were determined using the Maxwell construction. We found that at low densities, the layer is phase separated into a liquid droplet and a zero density gas. The range of this phase is 0.1270 to 0.1750 atom/Å². Gas-liquid coexistence ends at the equilibrium density for the liquid phase. This occurs at

0.1750 atom/Å², which is the density with the minimum energy per particle. This density was found to be insensitive to finite-size effects, and is in excellent agreement with the onset of superfluidity determined by torsional oscillator measurements. It is also consistent with heat capacity measurements. We demonstrated that the liquid phase in our simulation is superfluid, and we determined that the transition temperature was close to the value determined for a purely 2D superfluid at the same density.

The helium layer is uniformly covered in our simulation by the liquid phase from 0.1750 to 0.1905 atom/Å², at which point liquid-commensurate solid phase coexistence begins. The onset of this coexistence terminates superfluidity, since the growth of the solid phase disrupts the connectivity required to detect the superfluid. Experimentally, liquid-commensurate solid phase coexistence has been determined to begin at 0.1870 atom/Å² by both torsional oscillator and heat capacity measurements. We determined that the liquid phase is completely replaced by the $\sqrt{7} \times \sqrt{7}$ commensurate solid for densities above 0.1970 atom/Å², in good agreement with heat capacity measurements. Phase coexistence between the commensurate and incommensurate solid phases begins at 0.2032 atom/Å². For coverages above 0.2080 atom/Å², the incommensurate solid is the only phase occurring until layer promotion. These ranges for the solid coexistence and the incommensurate solid are in agreement with the heat capacity measurements. The density ranges for all the second layer phases described above are summarized in Fig. 8(a). Finally, we observed layer promotion for coverages above 0.2117 atom/Å², in excellent agreement with experiment.

ACKNOWLEDGMENTS

This work was supported in part by the National Aeronautics and Space Administration under Grant No. NAG3-1841. Some of the calculations for this work were performed using the computational facilities of the Supercomputer Computations Research Institute and the National High Magnetic Field Laboratory at the Florida State University. We wish to thank W. Magro and M. Boninsegni for allowing us to compare outputs of our program to theirs for the helium-helium high-temperature density matrix so that we could verify our solution. M. P. wishes to thank M. C. Gordillo for discussions on the superfluid transition temperature.

¹G. Zimmerli, G. Mistura, and M. H. W. Chan, Phys. Rev. Lett. **68**, 60 (1992).

²J. G. Dash and M. Schick, in *The Physics of Liquid and Solid Helium*, edited by K. H. Bennemann and J. B. Ketterson (Wiley, New York, 1978), pt. II.

³M. Schick, in *Phase Transitions in Surface Films*, edited by J. G. Dash and J. Ruvalds (Plenum, New York, 1980).

⁴D. S. Greywall and P. A. Busch, Phys. Rev. Lett. **67**, 3535 (1991).

⁵D. S. Greywall, Phys. Rev. B **47**, 309 (1993).

⁶M. Nielsen, J. P. McTague, and L. Passell, in *Phase Transitions in Surface Films*, edited by J. G. Dash and J. Ruvalds (Plenum, New York, 1980).

⁷K. Carneiro, L. Passell, W. Thomlinson, and H. Taub, Phys. Rev. B **24**, 1170 (1981).

⁸H. J. Lauter, H. Godfrin, V. L. P. Frank, and P. Leiderer, in *Phase Transitions in Surface Films 2*, edited by H. Taub, G. Torzo, H. J. Lauter, and S. C. Fain (Plenum, New York, 1991).

⁹H. J. Lauter, H. Godfrin, and P. Leiderer, J. Low Temp. Phys. **87**, 205 (1992).

¹⁰P. A. Crowell and J. D. Reppy, Phys. Rev. Lett. **70**, 3291 (1993).

¹¹P. A. Crowell and J. D. Reppy, Phys. Rev. B **53**, 2701 (1996).

¹²L. W. Bruch, M. W. Cole, and E. Zaremba, *Physical Adsorption: Forces and Phenomena* (Oxford, New York, 1997).

¹³M. Pierce and E. Manousakis, Phys. Rev. Lett. **81**, 156 (1998).

¹⁴M. Bretz, Phys. Rev. Lett. **31**, 1447 (1973).

- ¹⁵S. E. Polanco and M. Bretz, *Phys. Rev. B* **17**, 151 (1978).
- ¹⁶J. G. Dash, *Films on Solid Surfaces* (Academic, New York, 1975).
- ¹⁷V. Elser, *Phys. Rev. Lett.* **62**, 2405 (1989).
- ¹⁸F. F. Abraham, J. Q. Broughton, P. W. Leung, and V. Elser, *Europhys. Lett.* **12**, 107 (1990).
- ¹⁹P. A. Whitlock, G. V. Chester, and M. H. Kalos, *Phys. Rev. B* **38**, 2418 (1988).
- ²⁰M. C. Gordillo and D. M. Ceperley, *Phys. Rev. B* **58**, 6447 (1998).
- ²¹F. F. Abraham and J. Q. Broughton, *Phys. Rev. Lett.* **59**, 64 (1987).
- ²²P. A. Whitlock, G. V. Chester, and B. Krishnamachari, *Phys. Rev. B* **58**, 8704 (1998).
- ²³B. E. Clements, E. Krotscheck, and H. J. Lauter, *Phys. Rev. Lett.* **70**, 1287 (1993).
- ²⁴B. E. Clements, J. L. Epstein, E. Krotscheck, and M. Saarela, *Phys. Rev. B* **48**, 7450 (1993).
- ²⁵W. M. Saslow *et al.*, *Phys. Rev. B* **54**, 6532 (1996).
- ²⁶M. Wagner and D. M. Ceperley, *J. Low Temp. Phys.* **94**, 185 (1994).
- ²⁷M. Wagner and D. M. Ceperley, *J. Low Temp. Phys.* **102**, 275 (1996).
- ²⁸R. P. Feynman, *Phys. Rev.* **91**, 1291 (1953).
- ²⁹D. M. Ceperley, *Rev. Mod. Phys.* **67**, 279 (1995).
- ³⁰A. D. Novaco, *Phys. Rev. B* **13**, 3194 (1976).
- ³¹R. E. Ecke and J. G. Dash, *Phys. Rev. B* **28**, 3738 (1983).
- ³²R. A. Aziz *et al.*, *Mol. Phys.* **77**, 321 (1992).
- ³³D. M. Ceperley and E. L. Pollock, *Phys. Rev. Lett.* **56**, 351 (1986).
- ³⁴E. L. Pollock and D. M. Ceperley, *Phys. Rev. B* **36**, 8343 (1987).
- ³⁵E. L. Pollock and K. J. Runge, *Phys. Rev. B* **46**, 3535 (1992).
- ³⁶W. E. Carlos and M. W. Cole, *Surf. Sci.* **91**, 339 (1980).
- ³⁷W. H. Press, S. A. Teukolsky, W. T. Vetterling, and B. P. Flannery, *Numerical Recipes* (Cambridge, New York, 1992).
- ³⁸E. L. Pollock and D. M. Ceperley, *Phys. Rev. B* **30**, 2555 (1984).
- ³⁹M. P. Allen and D. J. Tildesley, *Computer Simulation of Liquids* (Oxford, New York, 1987).
- ⁴⁰N. Schultka and E. Manousakis, *Phys. Rev. B* **49**, 12 071 (1994).
- ⁴¹D. R. Nelson and J. M. Kosterlitz, *Phys. Rev. Lett.* **39**, 1201 (1977).